MagNeed – Needle-Shaped Electromagnets for Localized Actuation Within Compact Workspaces

Juan J. Huaroto, Michiel Richter, Mafalda Malafaia, Jayoung Kim, Chang-Sei Kim, *Senior Member, IEEE*, Jong-Oh Park, *Member, IEEE*, Jakub Sikorski, and Sarthak Misra, *Senior Member, IEEE*

***Abstract*—Electromagnetic actuation of micro-/milli-sized agents has traditionally relied on large electromagnets positioned at considerable distances from the agents. As a result, the electromagnets consume kilowatts of power to overcome the limited generation of magnetic field gradients. Miniaturized electromagnets offer an alternative approach for reducing power consumption via localized actuation of micro-/milli-sized agents. Typically, the generation of magnetic field gradients in the vicinity of a miniaturized electromagnet is comparable with traditional electromagnetic actuation systems. Miniaturized electromagnets can be positioned near target sites in microfluidic channels or *ex vivo* vasculatures. Thereby, localized trapping and actuation of magnetic micro-/milli-sized agents are carried out. This study introduces MagNeed – an electromagnetic actuation system composed of three needle-shaped electromagnets (NSEs). MagNeed can determine compact workspaces by positioning the NSEs at different spatial configurations. Each NSE generates magnetic field gradients (up to 3.5 T/m at 5 mm from the NSE tip axis) while keeping a maximum power consumption (0.5 W) and temperature (<42 °C). MagNeed is complemented by a framework that reconstructs the pose of the NSEs. Experiments test MagNeed and framework on a transparent Teflon tube (5 mm inner diameter). MagNeed demonstrates localized trapping and actuation of a 1 mm NdFeB bead against a flow of water and silica gel particles (1–3 mm diameter).**

***Index Terms*—Micro/nano robots, automation at micro-nano scales.**

Manuscript received 10 December 2022; accepted 20 April 2023. Date of publication 8 May 2023; date of current version 16 May 2023. This letter was recommended for publication by Associate Editor P. Song and Editor X. Liu upon evaluation of the reviewers' comments. This work was supported in part by the European Research Council (ERC) through the European Union's Horizon 2020 Research and Innovation Programme under Grant 866494 Project - MAESTRO, and in part by the Korea Health Technology Development R&D Project through the Korea Health Industry Development Institute and in part by the Ministry of Health and Welfare, Republic of Korea under Grant HI19C0642. *(Corresponding author: Juan J. Huaroto.)*

Juan J. Huaroto, Michiel Richter, Mafalda Malafaia, and Jakub Sikorski are with the Surgical Robotics Laboratory, Department of Biomechanical Engineering, University of Twente, 7522 NB Enschede, The Netherlands (e-mail: j.j.j.huarotosevilla@utwente.nl; m.richter@utwente.nl; mafalda.malafayao@gmail.com; j.sikorski@utwente.nl).

Jayoung Kim is with the Korea Institute of Medical Microrobotics, Gwangju 61011, Republic of Korea (e-mail: jaya@kimiro.re.kr).

Chang-Sei Kim is with the School of Mechanical Engineering, Chonnam National University, Gwangju 61186, Republic of Korea (e-mail: ckim@jnu.ac.kr).

Jong-Oh Park is with the Korea Institute of Medical Microrobotics, Gwangju 61011, Republic of Korea, and also with the School of Mechanical Engineering, Chonnam National University, Gwangju 61186, Republic of Korea (e-mail: jop@jnu.ac.kr).

Sarthak Misra is with the Surgical Robotics Laboratory, Department of Biomechanical Engineering, University of Twente, 7522 NB Enschede, The Netherlands, and also with Surgical Robotics Laboratory, Department of Biomedical Engineering, University Medical Centre Groningen, University of Groningen, 9713 AV Groningen, The Netherlands (e-mail: s.misra@utwente.nl).

This letter has supplementary downloadable material available at https://doi.org/10.1109/LRA.2023.3273519, provided by the authors.

Digital Object Identifier 10.1109/LRA.2023.3273519

CONTACTLESS actuation of micro-/milli-sized agents can open up novel treatments in medicine through autonomous navigation [1], targeted therapy [2], and surgery [3]. Among various contactless actuation methods (e.g., magnetic [4], acoustic [5], and thermocapillary [6]), remote magnetic manipulation has been proposed for propelling micro-/milli-sized agents within microfluidic channels and *ex vivo* vasculatures [7], [8]. Magnetic actuation excels in robust and precise control of micro/milli-sized agents [9], [10], [11], [12] by utilizing either permanent magnets or electromagnets distributed around a workspace [13].

The past decade has seen a rapid development of electromagnetic actuation systems for micro-/milli-robotic applications such as localized delivery of biological samples [14], micromanipulation of cells [15], and biopsy [16]. Such actuation systems require multiple electromagnets to allow multi-degrees of freedom actuation [10], [11]. In addition, various mathematical models have been proposed for design and calibration [17], [18], [19]. Electromagnetic actuation systems are primarily arrangements of stationary/mobile electromagnets surrounding a workspace [10], [11], [15], [20], [21], [22]. The traditional approach to designing electromagnetic actuation systems for micro-robotics follows the trend of using overscaled electromagnets. However, such systems can consume kilowatts of power, increasing the coil temperature and requiring additional cooling mechanisms [11], [20].

Recent developments in electromagnetic actuation have led to a continued interest in miniaturized electromagnets. The magnetic field gradient generated in the vicinity of a miniaturized electromagnet can be comparable to the values registered in traditional electromagnetic actuation systems [23]. Besides, power consumption is considerably reduced in three orders of magnitude [23], [24]. Studies on miniaturized electromagnets have proposed needle-like electromagnets to perform independent manipulation of magnetic micro-particles [25], [26]. An actuation system based on electromagnetic needles can provide direct access to enclosed regions. Furthermore, it can generate the force to actuate micro-/milli-sized agents while consuming less power and thus dissipating less heat than traditional systems.

In this study, we introduce MagNeed – an electromagnetic actuation system composed of three needle-shaped electromagnets (NSE). MagNeed creates a compact workspace by positioning the NSEs around a target site (Fig. 1). The system functionality

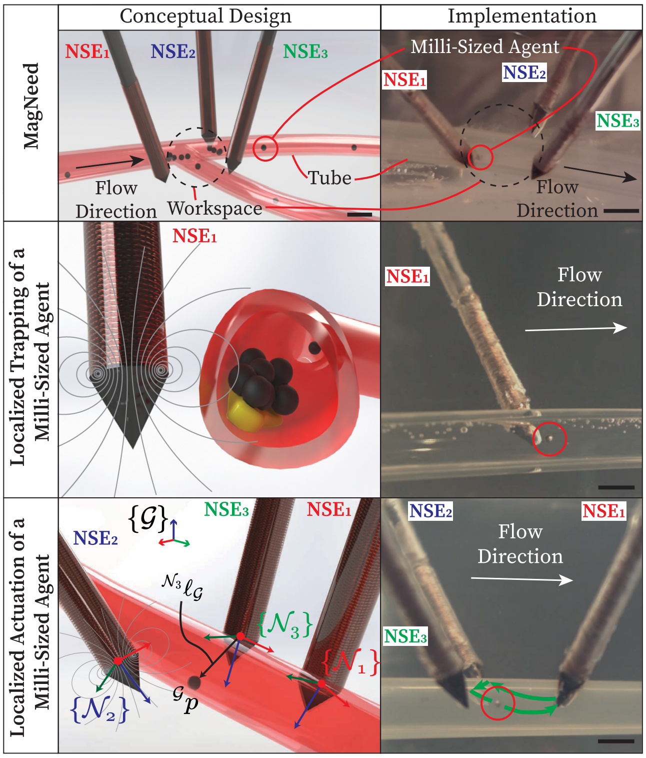

Fig. 1. Design concept and implementation of MagNeed: three needle-shaped electromagnets (NSEs) positioned around a Teflon tube to define a compact workspace that encloses a target site. A magnetic milli-sized agent is locally actuated in flowing liquid along the tube. Two applications are envisaged using single and three NSEs (MagNeed): localized trapping and localized actuation of a milli-sized agent. The NSEs frames are ($\{\mathcal{N}_1\}$, $\{\mathcal{N}_2\}$, and $\{\mathcal{N}_3\}$) and ($\{\mathcal{G}\}$) is the global reference frame. The vector (${}^{\mathcal{N}_3}\boldsymbol{\ell}_{\mathcal{G}}$) represents the distance between frame ($\{\mathcal{N}_3\}$) and the position of a milli-sized agent (${}^{\mathcal{G}}\boldsymbol{p}$) within the workspace. (All scale bars are 5 mm).

is validated by addressing two primary aims. (1) To demonstrate the use of NSEs for localized trapping/actuation of a milli-sized agent. (2) To provide a framework to reconstruct the pose of the NSEs. The study begins by introducing the design of MagNeed with an analytical model to describe the near magnetic field and gradients of the NSEs. We validate the analytical model utilizing our framework and magnetic field measurements. The remaining part of the study focuses on the experimental demonstration of MagNeed for localized trapping/actuation of a 1 mm NdFeB bead within a Teflon tube that transports water and silica gel particles.

I. System Overview

A. Design of MagNeed

MagNeed is a miniature electromagnetic actuation system to deploy localized actuation of micro-/milli-sized agents within a compact workspace. MagNeed consists of three needle-shaped electromagnets (NSEs) to permit magnetic field and/or gradient control in three-dimensional space [17]. The system development includes four steps: (i) the electromagnetic actuation strategy, (ii) the design of the NSEs, (iii) the current-to-field map to represent the near magnetic field and gradients generated by each NSE, (iv) the thermal analysis of the NSEs.

1) Electromagnetic Actuation Strategy: We begin the MagNeed development process by studying electromagnetic actuation principles in the context of micro-/milli-sized agents. The magnetic field generated by a needle-shaped electromagnet ($\boldsymbol{B}(\boldsymbol{p}, I)$) powered by an electrical current ($I \in \mathbb{R}$) exerts a wrench ($\boldsymbol{W} \in \mathbb{R}^6$) over a micro-/milli-sized agent with magnetic moment ($\boldsymbol{\mu} \in \mathbb{R}^3$) and located at a point ($\boldsymbol{p} \in \mathbb{R}^3$). $\boldsymbol{W}$ includes the magnetic force ($\boldsymbol{F} \in \mathbb{R}^3$) and magnetic torque ($\boldsymbol{T} \in \mathbb{R}^3$) and is defined as

$$\boldsymbol{W}(\boldsymbol{p}) = \begin{bmatrix} \boldsymbol{F}(\boldsymbol{p}) \\ \boldsymbol{T}(\boldsymbol{p}) \end{bmatrix} = \begin{bmatrix} \nabla(\boldsymbol{\mu} \cdot \boldsymbol{B}(\boldsymbol{p}, I)) \\ \boldsymbol{\mu} \times \boldsymbol{B}(\boldsymbol{p}, I) \end{bmatrix}. \tag{1}$$

Local frames ($\{\mathcal{N}_k\}$, for$k = 1, 2, 3$) are constructed for each NSE according to a global reference frame ($\{\mathcal{G}\}$) (Fig. 1). At a point, (${}^{\mathcal{G}}\boldsymbol{p} \in \mathbb{R}^3$) concerning the global reference frame, the magnetic field (${}^{\mathcal{G}}\boldsymbol{B}({}^{\mathcal{G}}\boldsymbol{p})$) is the sum of the magnetic field generated by each NSE (${}^{\mathcal{G}}\boldsymbol{B}_k({}^{\mathcal{G}}\boldsymbol{p})$). The unitary magnetic field (${}^{\mathcal{N}_k}\boldsymbol{\beta}_k({}^{\mathcal{N}_k}\boldsymbol{p})$) is generated concerning the local frame of the corresponding NSE. The NSEs are assumed to operate in their linear regions (i.e., the magnitude and components of the magnetic field vary linearly with the current). Hence, the magnetic field in local frames is defined as

$${}^{\mathcal{N}_k}\boldsymbol{B}_k({}^{\mathcal{N}_k}\boldsymbol{p}) = {}^{\mathcal{N}_k}\boldsymbol{\beta}_k({}^{\mathcal{N}_k}\boldsymbol{p}) I_k, \tag{2}$$

where $I_k \in \mathbb{R}$, is the current through the kth NSE. In order to compute the vectors ${}^{\mathcal{G}}\boldsymbol{B}_k({}^{\mathcal{G}}\boldsymbol{p})$, we define the rotation matrices (${}^{\mathcal{G}}\boldsymbol{R}_{\mathcal{N}_k} \in SO(3)$). This way, ${}^{\mathcal{N}_k}\boldsymbol{p} = {}^{\mathcal{N}_k}\boldsymbol{R}_{\mathcal{G}}\, {}^{\mathcal{G}}\boldsymbol{p} + {}^{\mathcal{N}_k}\boldsymbol{\ell}_{\mathcal{G}}$, where ${}^{\mathcal{N}_k}\boldsymbol{\ell}_{\mathcal{G}} \in \mathbb{R}^3$ are the vectors that represent the distances between the local and global frames (Fig. 1). Hence, ${}^{\mathcal{G}}\boldsymbol{B}_k({}^{\mathcal{G}}\boldsymbol{p})$ is computed as follows:

$${}^{\mathcal{G}}\boldsymbol{B}_k({}^{\mathcal{G}}\boldsymbol{p}) = {}^{\mathcal{G}}\boldsymbol{R}_{\mathcal{N}_k}\, {}^{\mathcal{N}_k}\boldsymbol{\beta}_k({}^{\mathcal{N}_k}\boldsymbol{p}) I_k. \tag{3}$$

According to magnetism principles, field and gradients generated by an electromagnet are stronger at closer distances [23]. MagNeed aims to achieve localized actuation of micro-/milli-sized agents by defining compact workspaces. Substituting (3) into (1), we obtain the magnetic force (${}^{\mathcal{G}}\boldsymbol{F}({}^{\mathcal{G}}\boldsymbol{p})$) exerted on a micro-/milli-sized agent located at ${}^{\mathcal{G}}\boldsymbol{p}$:

$${}^{\mathcal{G}}\boldsymbol{F}({}^{\mathcal{G}}\boldsymbol{p}) = \boldsymbol{\mu}^T \begin{bmatrix} \frac{\partial[{}^{\mathcal{G}}\boldsymbol{\beta}_1({}^{\mathcal{G}}\boldsymbol{p})]}{\partial x} & \dots & \frac{\partial[{}^{\mathcal{G}}\boldsymbol{\beta}_3({}^{\mathcal{G}}\boldsymbol{p})]}{\partial x} \\ \frac{\partial[{}^{\mathcal{G}}\boldsymbol{\beta}_1({}^{\mathcal{G}}\boldsymbol{p})]}{\partial y} & \dots & \frac{\partial[{}^{\mathcal{G}}\boldsymbol{\beta}_3({}^{\mathcal{G}}\boldsymbol{p})]}{\partial y} \\ \frac{\partial[{}^{\mathcal{G}}\boldsymbol{\beta}_1({}^{\mathcal{G}}\boldsymbol{p})]}{\partial z} & \dots & \frac{\partial[{}^{\mathcal{G}}\boldsymbol{\beta}_3({}^{\mathcal{G}}\boldsymbol{p})]}{\partial z} \end{bmatrix} \begin{bmatrix} I_1 \\ I_2 \\ I_3 \end{bmatrix}. \tag{4}$$

2) Needle-Shaped Electromagnets (NSEs): The second step in MagNeed development involves the design of NSEs capable of generating magnetic gradients to actuate a micro-/milli-sized agent. We compare the magnetic field gradients generated by two NSEs with different core tip geometries: conical and straight (Fig. 2(a)). Thereon, we study the optimal core ratio to maximize the magnetic gradients at the tip vicinity of an NSE.

The structure of the NSE follows a steel-cored coil design extended along a section ($l_c \in \mathbb{R}^+$) of the core length ($l_i \in \mathbb{R}^+$) (Fig. 2(a)). The central part of the NSE, made out of machined ferromagnetic steel, serves a double purpose. First, it gives

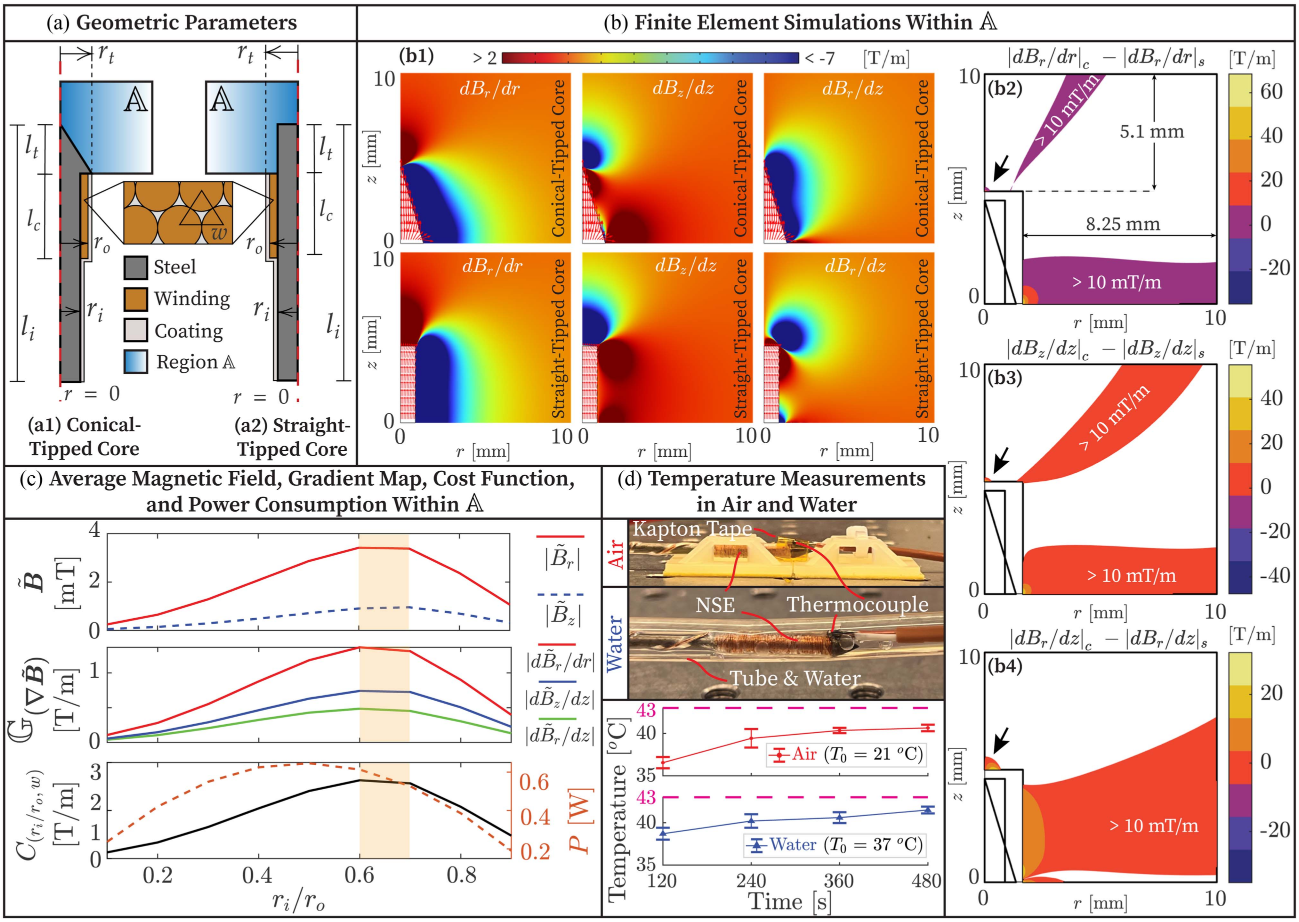

Fig. 2. Geometric and magnetic properties of needle-shaped electromagnets (NSEs) within MagNeed. a) Geometric parameters of two NSEs with different core tip geometries: conical (a1) and straight (a2). The geometry of the NSEs comprises three parts: steel core, copper winding, and polyolefin coating. The winding is arranged around the core into layers (magnified view), while the coating creates a physical interface between the NSE and the surrounding medium. The subscripts t, c, and i indicate tip, coil, and core, respectively. b) Finite element simulation within the region ($\mathbb{A} = \{r \wedge z \in \mathbb{R}_{\geq 0} : r \leq 10$ mm, $z \leq 10$ mm$\}$). The simulations are realized in finite element software (COMSOL Multiphysics 5.5, COMSOL AB, Sweden) using a current of 1 A. (b1) The magnetic gradients generated by the NSEs with conical and straight-tipped cores within the region ($\mathbb{A}$). (b2)–(b4) The differences of normalized gradients generated by the NSEs with conical ("c") and straight ("s") tipped cores. The differences are plotted within a sub-region of $\mathbb{A}$. The colored regions indicate differences greater than 10 mT/m. The triangle and rectangle at the bottom-left of the graphs indicate the conical and straight-tipped cores, respectively. The black arrows indicate the regions that are close to the tip core. c) Parametric optimization results to identify the optimal coil ratio (r_i/r_o), which maximizes the cost function ($C_{(r_i/r_o,w)}$) within $\mathbb{A}$. The colored region represents the optimal interval ($r_i/r_o \in [0.6, 0.7]$) using a wire diameter ($w = 0.2$ mm). d) Temperature measurements in ambient air (21 °C) and water (37 °C): the thermocouple probe is located in contact with the NSE tip. The temperature data is acquired using a digital multimeter (U1272 A, Keysight Technologies, USA). The NSE is powered using a constant current of 0.75 A for an interval of 480 s. The maximum temperature reported is less than 43 °C.

structural integrity. Second, it serves as an electromagnet core, amplifying the field generated by a copper solenoid wrapped around its distal part. Finally, an electrothermal coating of polyolefin (0.1 mm thick) wraps the body of the NSE to physically isolate it from the surrounding medium.

In order to visualize the magnetic gradients ($\frac{dB_r}{dr}$, $\frac{dB_z}{dz}$, $\frac{dB_r}{dz}$) generated by the NSEs with conical and straight-tipped cores, we performed finite element simulations within a region ($\mathbb{A}$) (Fig. 2(b1)). Table I provides the geometric parameters used in the simulations. To compare the gradients generated by the NSEs with conical and straight-tipped cores, we compute the differences: $|\frac{dB_r}{dr}|_c - |\frac{dB_r}{dr}|_s$, $|\frac{dB_z}{dz}|_c - |\frac{dB_z}{dz}|_s$, and $|\frac{dB_r}{dz}|_c - |\frac{dB_r}{dz}|_s$. The subscripts "c" and "s" stand for conical and straight-tipped cores, respectively. Figs. 2(b2)–(b4) show the regions where the differences are greater than 10 mT/m. The black arrow indicates that the NSE with a conical-tipped core improves the generation of gradients at short distances ($\leq$ 0.55 mm) from the core tip (along the z-axis) [27], [28]. Moreover, the base of the conical tip, with a radius ($r_t > r_i$), improves the generation of gradients along the r-axis (Figs. 2(b2)–(b4)).

TABLE I
GEOMETRIC PARAMETERS OF THE NEEDLE-SHAPED ELECTROMAGNETS (NSES)

Parameter	Symbol	Value
Core Radius	r_i	**0.875 mm**
Coil Radius	r_o	**1.25 mm**
Core Ratio	r_i/r_o	**0.7**
Tip Radius	r_t	**1.35 mm**
Tip Length	l_t	**4.5 mm**
Core Length	l_i	**100 mm**
Coil Length	l_c	**17.5 mm**
Number of Turns	n	**175**
Wire Diameter	w	**0.2 mm**

The simulation results indicate that the NSE with a conical-tipped core can generate strong gradients in the proximity of the core tip. In addition, the improved generation of magnetic gradients along the r-axis suggests that the NSEs can be used for in-/off-axis actuation. This study proposes an optimization-based design to maximize the magnetic field gradients generated by an NSE with a conical-tipped core. The optimization problem has two variables: core ratio ($r_i/r_o \in \mathbb{R}^+$) and wire diameter ($w \in \mathbb{R}^+$) to maximize a cost function ($C_{(r_i/r_o,w)} \in \mathbb{R}^+$), which includes the average intensity of the magnetic field gradient ($\nabla\tilde{\boldsymbol{B}} \in \mathbb{R}^{3\times3}$) within the region ($\mathbb{A}$) shown in Fig. 2(a). The function ($C_{(r_i/r_o,w)}$) is defined by the following expression:

$$C_{(r_i/r_o,w)} = \left|\left|\mathbb{G}_{(\nabla\tilde{\boldsymbol{B}})}\right|\right|_2, \tag{5}$$

where the gradient map ($\mathbb{G}_{(\nabla\tilde{\boldsymbol{B}})}$: $\mathbb{R}^{3\times3} \rightarrow \mathbb{R}^3$) is used to obtain the three independent and unequal components of the magnetic field gradient: $\mathbb{G}_{(\nabla\tilde{\boldsymbol{B}})} = [|\frac{d\tilde{B}_r}{dr}|, |\frac{d\tilde{B}_z}{dz}|, |\frac{d\tilde{B}_r}{dz}|]^T$. The following relationship [29]:

$$n = \left\lfloor \frac{l_c(r_o - r_i - w)2}{\sqrt{3}w^2} + \frac{l_c}{w} - \frac{(r_o - r_i - w)\sqrt{3}}{3w} - \frac{1}{2} \right\rfloor, \tag{6}$$

where $\lfloor\rfloor : \mathbb{R} \rightarrow \mathbb{Z}$ is the floor function, computes the maximum number of winding turns ($n \in \mathbb{Z}^+$). The wire diameter (w), the resistivity of the cooper wire ($\rho = 1.72\times10^{-8}$ Ω.m), the core radius (r_i), number of turns (n), and the simulation current (I = 1 A) are used to estimate the power consumption (P) of the NSE using the formula: $P = 8\,\rho\,r_i\,n/w^2$.

The simulations are carried out within a range of standard wire diameters (w = 0.1, 0.2, 0.3, 0.4 mm), an interval of core ratios (r_i/r_o = [0.1, 0.9]), and using a current of 1 A. The axis symmetry of the NSE leads to simplifying the 3D geometry into a 2D problem. Within the region ($\mathbb{A}$), the mesh is constructed using triangular elements (minimum size of 1 μ m) with an average mesh quality of 92%. According to the simulation results, the cost function tends to maximize for short wire diameters. However, there is a trade-off with the power consumption (P). In this study, we use a w = 0.2 mm diameter wire, which maximizes $C_{(r_i/r_o,w)}$ within the interval ($r_i/r_o \in$ [0.6, 0.7]), having a power consumption ($P \in$ [0.5, 0.6] W at 1 A) (Fig. 2(c)). For limiting the power consumption to 0.5 W, we chose $r_i/r_o = 0.7$, and the final dimensions of the NSE are provided in Table I.

3) Current-to-Field Map: The magnetic field generated by a needle-shaped electromagnet (NSE) is mapped into a current to reach magnetic actuation over a micro-/milli-sized agent. A high-resolution hall effect sensor (MLX90393, SparkFun Electronics, USA) mounted at the end effector of a collaborative 7-DoF robot (Panda, Franka Emika GmbH, Germany) acquires the magnetic field data within the NSE vicinity. The data is transferred to a microcontroller (Arduino DUE, Arduino, Italy) based on an Atmel SAM3X8E ARM Cortex-M3 CPU, using an I2C interface, and subsequently transmitted to a computer using a serial interface (sampling frequency of 100 Hz). A 3D printed support is used to hold the NSE horizontally while being powered with 1 A (Fig. 3(a)). A longitudinal scan along the

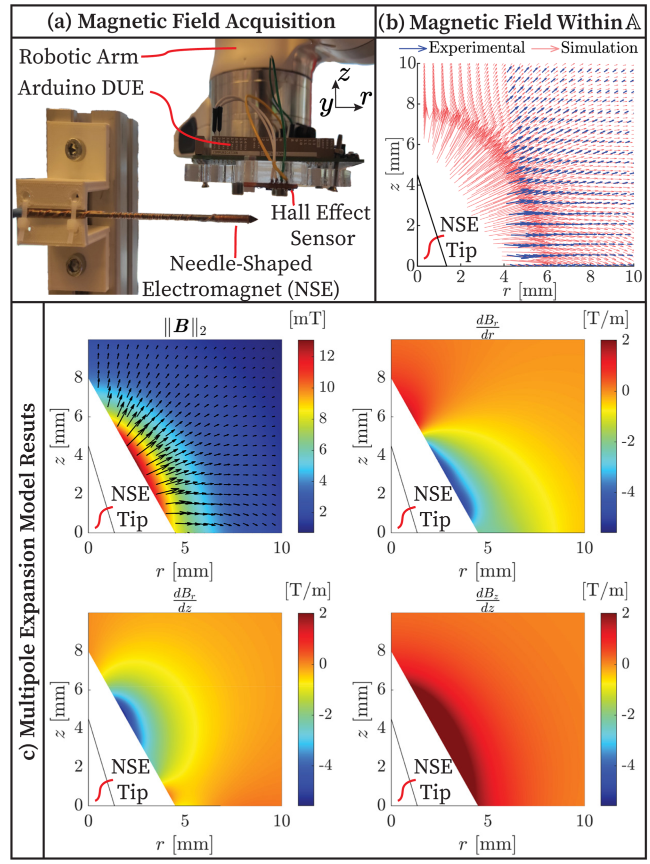

Fig. 3. Current-to-field map of a needle-shaped electromagnet (NSE): a) The magnetic field acquisition at the distal part of the NSE (i.e., region $\mathbb{A}$). b) Experimental and finite element data comparison ($R^2 = 0.9414$). c) The multipole expansion model fits the experimental and simulation data ($R^2 = 0.9986$ and $R^2 = 0.9913$ in the r- and z-axis, respectively). The magnetic field and the three non-zero gradient components are plotted using a current of 1 A. At the coordinates ([5, 0] mm), the magnitude of the magnetic field ($\|\boldsymbol{B}\|_2$) and the gradient components ($|\frac{dB_r}{dr}|$, $|\frac{dB_r}{dz}|$, $|\frac{dB_z}{dz}|$) reach values of 9 mT, 3.5 T/m, 0.09 T/m, and 1.02 T/m, respectively. At the coordinates ([10, 0] mm), magnetic field and gradient components are 2.1 mT, 0.42 T/m, 0.004 T/m, and 0.24 T/m, respectively. The triangle at the bottom-left of the graphs indicates the tip of the NSE.

y-axis is performed to identify the sagittal plane of the NSE (r-z plane). Thereon, a raster scan path is generated to acquire the magnetic field data in the r-z plane (Fig. 3(b)). In order to compute the current-to-field map, the data is bounded within the region ($\mathbb{A}$) using a multi-pole expansion defined by a non-linear scalar potential function ($\Psi(\boldsymbol{p})$) [19]:

$$\boldsymbol{B}(\boldsymbol{p}, I) = \nabla\Psi(\boldsymbol{p})I. \tag{7}$$

The unitary magnetic field ($\boldsymbol{\beta}(\boldsymbol{p}) \in \mathbb{R}^3$) and its corresponding gradient ($\nabla\boldsymbol{\beta}(\boldsymbol{p}) \in \mathbb{R}^{3\times3}$) at a fitting current ($I_f$ = 1 A) are defined as follows

$$\begin{cases} \boldsymbol{\beta}(\boldsymbol{p}) = \frac{\nabla\Psi(\boldsymbol{p})}{I_f} \\ \nabla\boldsymbol{\beta}(\boldsymbol{p}) = \left[\frac{\partial\boldsymbol{\beta}(\boldsymbol{p})}{\partial x}, \frac{\partial\boldsymbol{\beta}(\boldsymbol{p})}{\partial y}, \frac{\partial\boldsymbol{\beta}(\boldsymbol{p})}{\partial z}\right]. \end{cases} \tag{8}$$

Substituting (8) in (7), we obtain the current-to-field map for each NSE. The multi-pole model fits the magnetic field data from experimental and simulation results (Fig. 3(b)). Yet, the model

TABLE II
MAGNEED SPECIFICATIONS: VALUES PER NEEDLE-SHAPED ELECTROMAGNET (NSE)

Specifications	Value
Maximum Power [W]	**0.5**
Power per Unit Area Dissipation [mW/mm^2]	**3.9**
Magnetic Field (at 5 mm from tip axis) [mT]	**9**
Magnetic Field Gradient (at 5 mm from tip axis) [T/m]	**3.5**
Number of NSEs	**3**
Maximum Current [A]	**0.75**
Electrical Resistance [Ω]	**0.84**
Operating Temperature [^{o}C]	$<$ **42**
Workspace per NSE: Cylinder (radius & height) [mm]	**(10 & 10)**

starts to lack correlation ($R^2 < 0.9$) for coordinates $r < 5$ mm and $z < 8$ mm. Beyond region ($\mathbb{A}$), the magnetic field and gradients tend to zero, which implies that the workspace of an NSE has the shape of a cylinder (radius and height of 10 mm) (Fig. 3(c)).

4) Thermal Analysis: Limiting the maximum temperature of the needle-shaped electromagnets (NSEs) to a physiologically permissible value (43 °C) is essential for reducing thermal perturbations in microfluidic channels or *ex vivo* vasculatures. We experimentally test the surface temperature of an NSE by powering it with 0.75 A. The temperature is acquired in ambient air (21 °C) and water (37 °C) using a thermocouple probe in contact with the NSE. Fig. 2(d) shows the experimental setup and temperature results for an interval of 480 s. The experimental results show that the temperature reaches a saturation point ($<$ 42 °C). Further experiments with currents ($>$ 0.75 A) at least doubled the temperature of the NSEs. Thus, we set 0.75 A as the maximum operating current of MagNeed.

5) Final MagNeed Design: The four previous steps served as foundations to determine the design and features of MagNeed. Table II provides the main characteristics of MagNeed. We highlight the low-power consumption, operating temperature, and magnetic field gradients, which are comparable with state-of-the-art macroscale electromagnetic actuation systems [10], [11], [20], [21], [22], [23], [24].

B. MagNeed Framework

MagNeed can generate different workspace layouts depending on the spatial configuration of the needle-shaped electromagnets (NSEs). Consequently, the system is complemented by providing a framework to reconstruct the pose of the NSEs according to a global reference frame ($\{\mathcal{G}\}$) (Fig. 4). The pose reconstruction utilizes depth maps and points cloud data to estimate the pose of optical markers attached to the NSE. The data are acquired by a 3D camera (Realsense SR305, Intel, USA) mounted at the end effector of a collaborative 7-DoF robot (Panda, Franka Emika GmbH, Germany). The optical markers are attached at 70 mm from the origin of coordinates of each NSE (Fig. 4). A post-processing algorithm is implemented in MATLAB (version R2021b, MathWorks, USA) to compute the pose of the optical markers and NSEs [30].

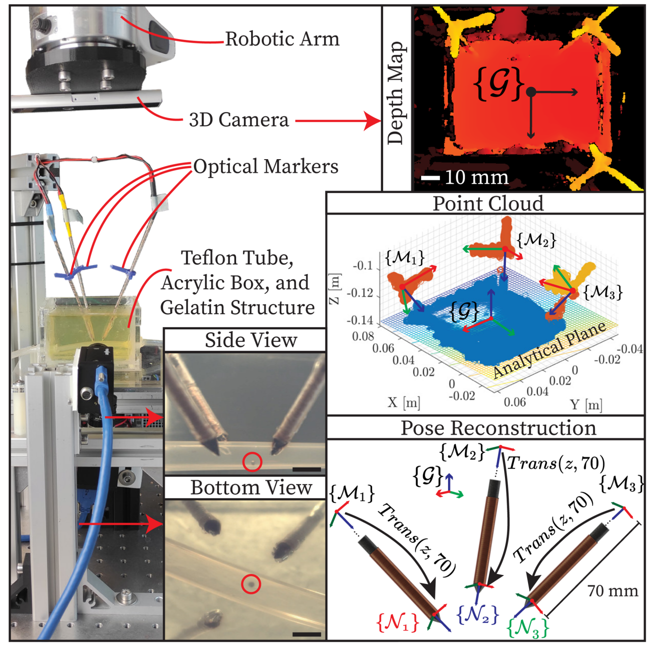

Fig. 4. Experimental setup to locally actuate a 1 mm NdFeB bead within the Teflon tube. The tube ends are connected to two syringes that can be used to manually or automatically pump water. The current applied to the needle-shaped electromagnets (NSEs) is controlled through servo drives (iPOS4808 BX-CAT, Technosoft S.A., Switzerland). The servo drives are connected to a computer (running Linux Ubuntu 18.04, kernel version 4.19, NVidia QUADRO M2000 M GPU, and 32 GB RAM) through an EtherCAT network (control rate of 500 Hz). The imaging of the magnetic bead is acquired by two cameras (grasshopper 3, Teledyne FLIR, USA), which are placed at the bottom and side of the acrylic box. Objective lenses (DF6HA-1S, FUJINON lenses, USA) are assembled to improve the image resolution (350 µ m per pixel) in a field of view of 1024 × 1024 pixels^2. Both cameras are connected to the computer via USB 3.1, and a C++ program is implemented using OpenCV 4.5 to simultaneously record videos (acquisition rate of 30 frames per second). The red circles enclose the magnetic bead utilized in the experiments. (The black scale bars are 5 mm). The pose reconstruction of the NSEs uses a 3D camera to acquire depth images and point cloud data. Optical markers are attached at 70 mm from the NSE frames ($\{\mathcal{N}_k\}$, for $k = 1, 2, 3$). The global reference frame ($\{\mathcal{G}\}$), defined on top of the gelatin structure, is identified by fitting the point cloud to an analytical plane equation. The optical marker frames ($\{\mathcal{M}_k\}$, for $k = 1, 2, 3$) are computed by fitting the point cloud to three orthogonal vectors. Finally, a Euclidean translation from ($\{\mathcal{M}_k\}$) to ($\{\mathcal{N}_k\}$) determines the pose of the NSEs. (The color maps indicate the proximity of the point cloud to the 3D camera).

C. MagNeed Model Validation

The framework is initially tested using a 3D printed structure with three symmetrically spaced cavities to hold the needle-shaped electromagnets (NSEs) (Fig. 5(a)). The results of the pose reconstruction showed a maximum error of 6% regarding the inclination angle of the NSEs (50°). An additional cavity holds a high-precision teslameter probe (3MH3A-500MT, Senis AG, Baar, Switzerland). The teslameter is connected to a computer using a serial interface (acquisition frequency of 125 Hz). The NSEs are powered using sinusoidal currents (amplitude of 0.75 A) while the teslameter probe acquires the magnetic field components (B_x, B_y, and B_z). Fig. 5(b) shows the simulated and experimental values of the magnetic field. The error between the experiment and model reaches a maximum of 26.12% corresponding to the z-axis and remains less than 9% for the other axis. We explain such results according to the error

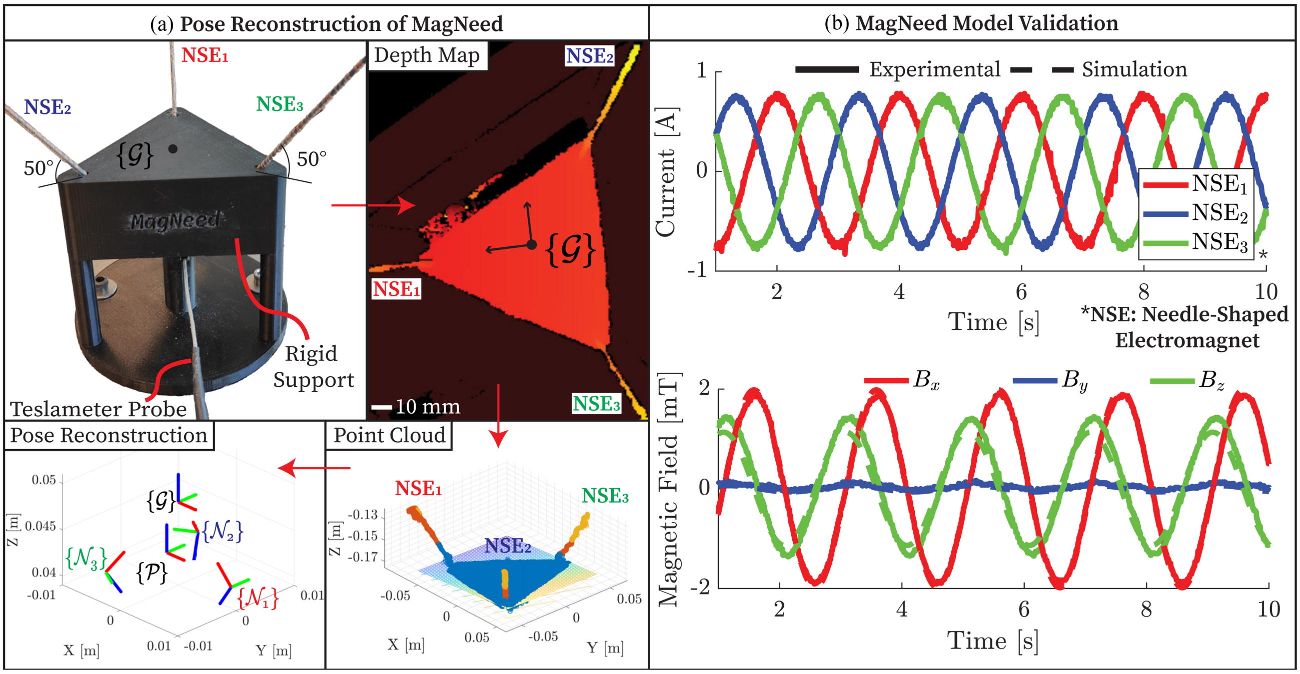

Fig. 5. a) Pose reconstruction of MagNeed: the rigid support permits the placement of the needle-shaped electromagnets (NSE) and a high-precision teslameter probe (3MH3A-500MT, Senis AG, Switzerland). A 3D camera, located above the rigid support, acquires the depth map and point cloud data of the NSEs and surroundings. The acquired data are used to compute the pose of the NSEs, which are represented by the local frames ($\{\mathcal{N}_1\}$, $\{\mathcal{N}_2\}$, $\{\mathcal{N}_3\}$). The global reference frame ($\{\mathcal{G}\}$) is identified on top of the rigid support. (The color maps indicate the proximity of the point cloud to the 3D camera). b) MagNeed model validation using sinusoidal currents (amplitude: 0.75 A, frequency: 0.5 Hz, phases: 0, $-2\pi/3$, $2\pi/3$) on each NSE. The components (B_x, B_y, and B_z) of the magnetic field ($\boldsymbol{B}$) are acquired according to the teslameter probe frame ($\{\mathcal{P}\}$). The root mean square (RMS) error between simulation and experiments, according to B_x, B_y, and B_z signals, are 0.0047, 0.04, and 0.05, respectively.

propagation from the pose reconstruction. The model correlation is biased by the maximum error values, which are registered at the peak/trough points of the magnetic field results (Fig. 5(b)). However, overall the model fits the magnetic field behavior evidence of the root mean square (RMS) error values obtained for each component of the magnetic field ($\boldsymbol{B}$) (Fig. 5(b)).

II. Experimental Demonstrations

MagNeed is tested on a Teflon tube (5 mm inner diameter) that transports water, a 1 mm NdFeB bead (SP0100-50, SuperMagnetMan, USA), and non-magnetic particles (silica gel particles of 1-3 mm diameter). The needle-shaped electromagnets (NSEs) are positioned around the tube, which is assembled within an acrylic box (70 $\times$ 90 $\times$ 60 mm ^{3}). A gelatin structure is cured within the acrylic box to hold the NSEs in a constant spatial configuration (Fig. 4). The gelatin structure is fabricated by mixing 15% (by-weight) porcine gelatin powder (Dr. Oetker, Germany) with 85% water. The blend is heated up to a temperature of 70 $^\circ$ C to dissolve the gelatin powder. Finally, the blend is poured into the acrylic box and cured at room temperature. The experiments are conducted using a setup (Fig. 4) designed for visualizing/tracking the magnetic bead, controlling the current, and reconstructing the pose of the NSEs. In order to test the near magnetic field gradients produced by the NSEs, we create a flow of water and silica gel particles within the tube. This section demonstrates experimentally the localized trapping and actuation applications shown in Fig. 1. *Please refer to the supplementary video for the demonstration of these experiments.*

A. Localized Trapping of a Milli-Sized Agent

This experiment shows the potential of a single needle-shaped electromagnet (NSE) for localized trapping of micro-/milli-sized agents in the perfusion of fluid within a microfluidic channel or *ex vivo* vasculatures. We compare the performance and power consumption required to trap a magnetic bead using an NSE and an electromagnetic system composed of 9 coils [11]. A syringe pump (NE-4000, New Era Pump Systems, USA) is used to transport water and milli-sized agents (the 1 mm NdFeB bead and silica gel particles) at a constant flow rate of 100 ml/min. Both NSE and electromagnetic system generate a magnetic force that pulls the magnetic bead to the inner wall of the tube. Our results show that the NSE can efficiently trap a magnetic bead while consuming 8 mW (using 0.1 A) compared to the 2827 mW of the electromagnetic system. The trapping performance using the NSE is also tested by manually pumping water and silica gel particles (Fig. 6(a)). Manual pumping permits the generation of flow rate peaks that cannot be recreated with the syringe pump. Using digital image processing, we acquire the peak speed of the silica gel particles. Hence, the peak flow rate of fluid flow is approximately 376 ml/min. Our results show that the magnetic

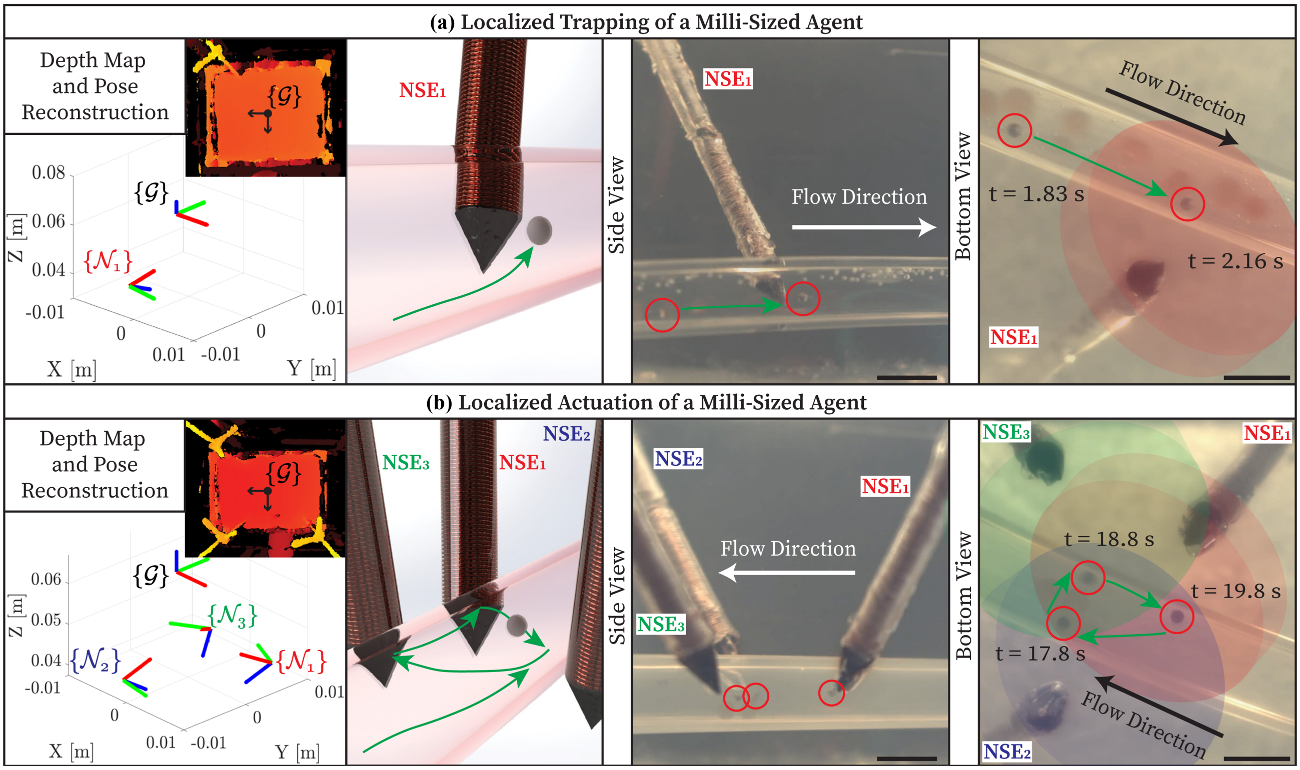

Fig. 6. Localized trapping and actuation of a 1 mm NdFeB bead within a transparent Teflon tube. a) The magnetic bead moves downstream (t = 1.83 s), then the force generated by a single needle-shaped electromagnet (NSE) (steady current of 0.5 A) pulls the bead toward the inner wall of the tube (t = 2.16 s). The NSE efficiently traps the bead against the flow of water and silica gel particles. b) The magnetic bead performs a periodic motion among three points within the MagNeed workspace while a flow of water and silica gel particles is created along the tube. The NSEs are activated in a round-robin manner ($f = 0.25$ Hz, duty cycle = 33%, and amplitude of 0.75 A). The red circle encloses the 1 mm NdFeB bead utilized in the experiments. The colored regions at the bottom view illustrate the workspace of each NSE. (All scale bars are 5 mm).

bead is efficiently trapped and holds its position, while the NSE has a power consumption of 0.21 W (using 0.25 A).

B. Localized Actuation of a Milli-Sized Agent

In this part of the study, we use MagNeed to actuate a magnetic bead. Each needle-shaped electromagnet (NSE) composing MagNeed has a workspace that covers the Teflon tube region (Fig. 6). Here, we show two experiments using MagNeed with a maximum power consumption of 0.5 W. (1) Localized actuation of a magnetic bead against a water flow and silica gel particles. (2) The interaction between a magnetic bead and silica gel particles in still water.

In the first experiment, the NSEs are activated in a round-robin manner. Simultaneously, water and silica gel particles are manually pumped along the tube (peak flow rate is approximately 114 ml/min) (Fig. 6(b)). We observe that the magnetic bead tends to perform a periodic motion. Yet, when using a low actuation frequency ($f = 0.25$ Hz), the magnetic bead is prone to interact with the silica beads and follow the flow direction. By increasing the actuation frequency up to $f = 1$ Hz, the magnetic bead tends to keep its direction of motion against the flow direction (peak flow rate is approximately 233 ml/min). The capability of MagNeed to actuate a magnetic bead against a flow of water and silica gel particles suggests that our system can be suitable for *ex vivo* experiments using micro-agents in physiological fluid [7].

In the second experiment, we aim to test the force exerted on a magnetic bead to interact with silica gel particles in still water. The magnetic bead and particles are positioned within the Teflon tube, which is surrounded by MagNeed. The NSEs are powered in a round-robin manner using the same currents but a higher frequency ($f = 9$ Hz, duty cycle = 33%, and amplitude of 0.75 A). As a result, the magnetic bead experiences an uncontrolled motion, which is used to collide with and move the silica gel particles. Although the magnetic forces scale with the volume of the magnetic object, MagNeed can generate strong pulling forces that could be applied for impact-based interaction with soft tissues [3].

III. Conclusions

This study introduces MagNeed – an electromagnetic actuation system that can determine a compact workspace around a target site using three needle-shaped electromagnets (NSEs). We propose an NSE design and an analytical model to represent the near magnetic field and gradients. Each NSE has a workspace in the shape of a cylinder (radius and height of 10 mm). The overall workspace of MagNeed is determined by the pose of the NSEs, which are computed using a reconstruction framework. The use of NSEs enables the generation of magnetic gradients (up to 3.5 T/m at 5 mm from the NSE tip axis) that are comparable to those produced by state-of-the-art electromagnetic actuation systems. The surface temperature of an NSE is less than 42 °C, making MagNeed suitable for *in vitro* and *ex vivo* applications. We experimentally demonstrate the capabilities of MagNeed to locally trap and actuate a 1 mm NdFeB bead within a narrow tube that transports water and silica gel particles. Our results show that MagNeed keeps a maximum power consumption of 0.5 W.

Future studies include the steering of micro-/milli-sized agents using clinical imaging modalities (e.g., ultrasound, computed tomography) as feedback. We also plan to reduce the pose reconstruction uncertainty by implementing a real-time algorithm to classify the point cloud. Moreover, a cell toxicity study testing different bio-compatible coating materials is required to utilize MagNeed in contact with biological tissue. Finally, studying the magnetic field properties by reducing the NSE dimensions and modifying the core materials could lead to flexible NSE potentially applicable for laparoscopy-/endoscopy-assisted navigation of micro-agents.

References

[1] S. Ornes, "Inner workings: Medical microrobots have potential in surgery, therapy, imaging, and diagnostics," *Proc. Nat. Acad. Sci.*, vol. 114, no. 47, pp. 12356–12358, 2017.

[2] B. Sun, G. Wood, and S. Miyashita, "Milestones for autonomous invivo microrobots in medical applications," *Surgery*, vol. 169, no. 4, pp. 755–758, 2021.

[3] O. Erin et al., "Overcoming the force limitations of magnetic robotic surgery: Magnetic pulse actuated collisions for tissue-penetrating-needle for tetherless interventions," *Adv. Intell. Syst.*, vol. 4, no. 6, 2022, Art. no. 2200072.

[4] J. J. Abbott, E. Diller, and A. J. Petruska, "Magnetic methods in robotics," *Annu. Rev. Control Robot. Auton. Syst.*, vol. 3, no. 1, pp. 57–90, 2020.

[5] S. Mohanty, A. Paul, P. M. Matos, J. Zhang, J. Sikorski, and S. Misra, "CeFlowBot: A biomimetic flow-driven microrobot that navigates under magneto-acoustic fields," *Small*, vol. 18, no. 9, 2022, Art. no. 2105829.

[6] F. N. Piñan Basualdo, A. Bolopion, M. Gauthier, and P. Lambert, "A microrobotic platform actuated by thermocapillary flows for manipulation at the air-water interface," *Sci. Robot.*, vol. 6, no. 52, 2021, Art. no. eabd 3557.

[7] B. Wang et al., "Endoscopy-assisted magnetic navigation of biohybrid soft microrobots with rapid endoluminal delivery and imaging," *Sci. Robot.*, vol. 6, no. 52, 2021, Art. no. eabd 2813.

[8] S. Lee et al., "A needle-type microrobot for targeted drug delivery by affixing to a microtissue," *Adv. Healthcare Mater.*, vol. 9, no. 7, 2020, Art. no. 1901697.

[9] G. Z. Lum et al., "Shape-programmable magnetic soft matter," *Proc. Nat. Acad. Sci.*, vol. 113, no. 41, pp. E6007–E6015, 2016.

[10] E. Diller, J. Giltinan, G. Z. Lum, Z. Ye, and M. Sitti, "Six-degree-of-freedom magnetic actuation for wireless microrobotics," *Int. J. Robot. Res.*, vol. 35, no. 1-3, pp. 114–128, 2016.

[11] F. Ongaro, S. Pane, S. Scheggi, and S. Misra, "Design of an electromagnetic setup for independent three-dimensional control of pairs of identical and nonidentical microrobots," *IEEE Trans. Robot.*, vol. 35, no. 1, pp. 174–183, Feb. 2019.

[12] Q. Wang, L. Yang, and L. Zhang, "Micromanipulation using reconfigurable self-assembled magnetic droplets with needle guidance," *IEEE Trans. Automat. Sci. Eng.*, vol. 19, no. 2, pp. 759–771, Apr. 2022.

[13] R. Chen, D. Folio, and A. Ferreira, "Analysis and comparison of electromagnetic microrobotic platforms for biomedical applications," *Appl. Sci.*, vol. 12, no. 1, 2022, Art. no. 456.

[14] H. Lee, A. Purdon, and R. Westervelt, "Manipulation of biological cells using a microelectromagnet matrix," *Appl. Phys. Lett.*, vol. 85, no. 6, pp. 1063–1065, 2004.

[15] B. Panigrahi, C.-H. Lu, N. Ghayal, and C.-Y. Chen, "Sperm activation through orbital and self-axis revolutions using an artificial cilia embedded serpentine microfluidic platform," *Sci. Rep.*, vol. 8, no. 1, pp. 1–9, 2018.

[16] Q. Jin, Y. Yang, J. A. Jackson, C. Yoon, and D. H. Gracias, "Untethered single cell grippers for active biopsy," *Nano Lett.*, vol. 20, no. 7, pp. 5383–5390, 2020.

[17] A. J. Petruska and B. J. Nelson, "Minimum bounds on the number of electromagnets required for remote magnetic manipulation," *IEEE Trans. Robot.*, vol. 31, no. 3, pp. 714–722, Jun. 2015.

[18] A. J. Petruska, J. Edelmann, and B. J. Nelson, "Model-based calibration for magnetic manipulation," *IEEE Trans. Magn.*, vol. 53, no. 7, pp. 1–6, Jul. 2017.

[19] M. Richter, V. K. Venkiteswaran, and S. Misra, "Multi-point orientation control of discretely-magnetized continuum manipulators," *IEEE Robot. Automat. Lett.*, vol. 6, no. 2, pp. 3607–3614, Apr. 2021.

[20] M. P. Kummer, J. J. Abbott, B. E. Kratochvil, R. Borer, A. Sengul, and B. J. Nelson, "OctoMag: An electromagnetic system for 5-DOF wireless micromanipulation," *IEEE Trans. Robot.*, vol. 26, no. 6, pp. 1006–1017, Dec. 2010.

[21] F. Niu, J. Li, W. Ma, J. Yang, and D. Sun, "Development of an enhanced electromagnetic actuation system with enlarged workspace," *IEEE/ASME Trans. Mechatron.*, vol. 22, no. 5, pp. 2265–2276, Oct. 2017.

[22] L. Yang, X. Du, E. Yu, D. Jin, and L. Zhang, "DeltaMag: An electromagnetic manipulation system with parallel mobile coils," in *Proc. Int. Conf. Robot. Automat*., 2019, pp. 9814–9820.

[23] J. Sikorski, S. Mohanty, and S. Misra, "MILiMAC: Flexible catheter with miniaturized electromagnets as a small-footprint system for microrobotic tasks," *IEEE Robot. Automat. Lett.*, vol. 5, no. 4, pp. 5260–5267, Oct. 2020.

[24] B. V. Johnson, N. Esantsi, and D. J. Cappelleri, "Design of the μMAZE platform and microrobots for independent control and micromanipulation tasks," *IEEE Robot. Automat. Lett.*, vol. 5, no. 4, pp. 5677–5684, Oct. 2020.

[25] J.-A. Seon, Z. Cenev, and Q. Zhou, "Automatic noncontact extraction and independent manipulation of magnetic particles using electromagnetic needle," *IEEE/ASME Trans. Mechatron.*, vol. 25, no. 2, pp. 931–941, Apr. 2020.

[26] O. Işıtman, H. Bettahar, and Q. Zhou, "Non-contact cooperative manipulation of magnetic microparticles using two robotic electromagnetic needles," *IEEE Robot. Automat. Lett.*, vol. 7, no. 2, pp. 1605–1611, Apr. 2022.

[27] B. D. Matthews, D. A. LaVan, D. R. Overby, J. Karavitis, and D. E. Ingber, "Electromagnetic needles with submicron pole tip radii for nanomanipulation of biomolecules and living cells," *Appl. Phys. Lett.*, vol. 85, no. 14, pp. 2968–2970, 2004.

[28] Y. Xiang, J. Miller, V. Sica, and D. A. LaVan, "Optimization of force produced by electromagnet needles acting on superparamagnetic microparticles," *Appl. Phys. Lett.*, vol. 92, no. 12, 2008, Art. no. 124104.

[29] J. Sikorski, C. M. Heunis, F. Franco, and S. Misra, "The ARMM system: An optimized mobile electromagnetic coil for non-linear actuation of flexible surgical instruments," *IEEE Trans. Magn.*, vol. 55, no. 9, pp. 1–9, Sep. 2019.

[30] F. Suligoj, C. M. Heunis, J. Sikorski, and S. Misra, "RobUSt–an autonomous robotic ultrasound system for medical imaging," *IEEE Access*, vol. 9, pp. 67456–67465, 2021.